ADVANCED FUNCTIONAL MATERIALS
www.afm-journal.de

Elephant Trunk Inspired Multimodal Deformations and Movements of Soft Robotic Arms

*Sophie Leanza, Juliana Lu-Yang, Bartosz Kaczmarski, Shuai Wu, Ellen Kuhl, and Ruike Renee Zhao**

Elephant trunks are capable of complex, multimodal deformations, allowing them to perform task-oriented high-degree-of-freedom (DOF) movements pertinent to the field of soft actuators. Despite recent advances, most soft actuators can only achieve one or two deformation modes, limiting their motion range and applications. Inspired by the elephant trunk musculature, a liquid crystal elastomer (LCE)-based multi-fiber design strategy is proposed for soft robotic arms in which a discrete number of artificial muscle fibers can be selectively actuated, achieving multimodal deformations and transitions between modes for continuous movements. Through experiments, finite element analysis (FEA), and a theoretical model, the influence of LCE fiber design on the achievable deformations, movements, and reachability of trunk-inspired robotic arms is studied. Fiber geometry is parametrically investigated for 2-fiber robotic arms and the tilting and bending of these arms is characterized. A 3-fiber robotic arm is additionally studied with a simplified fiber arrangement analogous to that of an actual elephant trunk. The remarkably broad range of deformations and the reachability of the arm are discussed, alongside transitions between deformation modes for functional movements. It is anticipated that this design and actuation strategy will serve as a robust method to realize high-DOF soft actuators for various engineering applications.

1. Introduction

Soft robots and soft actuators,[1] due to their compliant nature and ability to achieve smooth, continuous configurations and movements, have proven to be advantageous for use as delicate grippers and manipulators,[2] for biomimetic or bioinspired systems,[2c,3] and for biomedical applications.[4] To design soft robotic actuation strategies, many real-life biological structures have been investigated as inspiration. Muscular hydrostats, such as the elephant trunk and the octopus arm, are of particular interest to the scientific community as they can precisely achieve a magnificent array of multimodal deformations, including shortening, elongation, bending, twisting, as well as coupling of these behaviors (**Figure 1A**). The elephant trunk, in particular, is one of the largest actuators in the animal kingdom and can achieve rich and dexterous deformations due to the contraction of different muscles among the trunk's complex architecture.[5] Specifically, the trunk's movements are dictated by tens of thousands of muscle bundles arranged in different manners, for example, longitudinal and oblique ones (Figure 1B).[6] With the recent popularity of soft robotic systems, there exists a unique opportunity to study the elephant trunk for potential applications as high-degree-of-freedom (DOF) soft manipulators.

Considering the elephant trunk as a dexterous appendage, the trunk is used to perform necessary functions such as grabbing food and moving objects. Accordingly, the task-oriented movements performed by trunks require the generation of a series of distinct deformation modes, along with the ability to transition between these modes in a controlled manner. There is a considerable body of work regarding soft robotic arms aiming to mimic muscular hydrostats such as the elephant trunk. These works largely utilize cylindrical structures with either strain-limiting strips or fibers,[7] expandable compartments,[8] or contractible materials[9] arranged in helical, longitudinal, or circumferential manners, to generate elongation, contraction, twisting, or bending upon an applied input. Many of these actuators are split into piecewise segments that are actuated independently, complicating their control.[7a,d,f,8c–e] Others utilize porous structures[10] or multi-unit structures with reconfigurable building blocks[11] to achieve different types of bending. Although there are many different explored designs, most can only achieve one or two deformation modes per actuator, which is a limitation inherent to the design and coupled actuation strategy. While a few previously studied soft actuators can achieve multimodal deformation,[7a,f,8b,c,9a] the ability of soft robotic arms to transition between different deformation modes to generate functional movements is largely unexplored. Thus, it is highly desired to develop better design strategies that incorporate actuation mechanisms for integrated bending, twisting, and contraction, into one robotic arm, as well as corresponding strategies for controlling the functional transitioning between different modes.

S. Leanza, J. Lu-Yang, B. Kaczmarski, S. Wu, E. Kuhl, R. R. Zhao
Stanford University
Stanford, CA 94305, USA
E-mail: rrzhao@stanford.edu
The ORCID identification number(s) for the author(s) of this article can be found under https://doi.org/10.1002/adfm.202400396

DOI: 10.1002/adfm.202400396

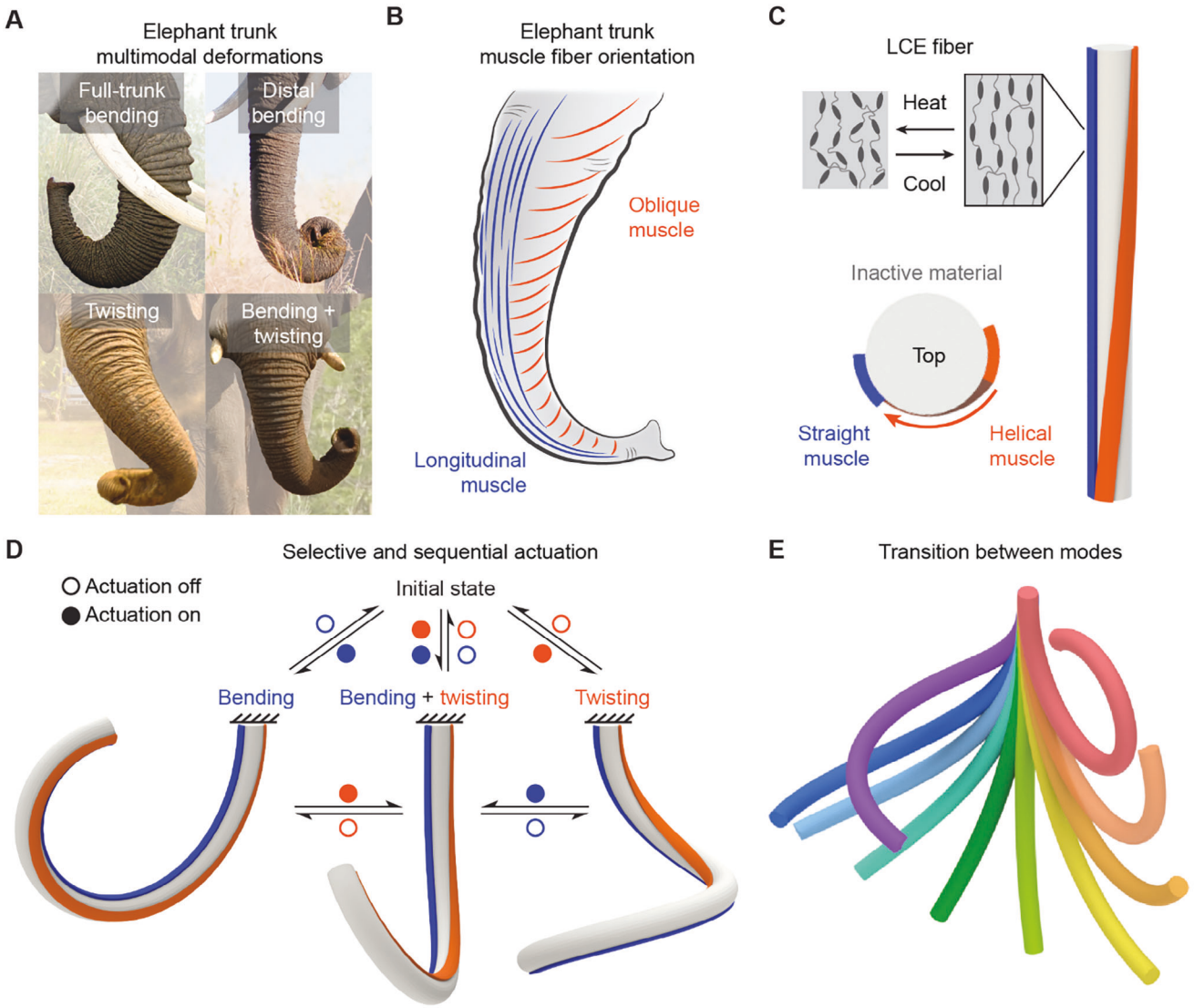

Figure 1. Elephant trunk multimodal deformation and a trunk-inspired soft robotic arm strategy. A) Multimodal deformations of elephant trunks, including full-trunk bending, distal bending, twisting, and coupled bending and twisting. B) Schematic of the muscle fiber orientations of an elephant trunk, including longitudinal and oblique muscle fibers. C) Schematic of the elephant trunk-inspired soft robotic arm design. LCE muscle fibers (blue and orange) are patterned along an inactive (gray) elastomer rod. The LCE fibers contract when being heated and return to their initial configuration upon cooling. D) Schematic for the selective and sequential actuation of LCE fibers to achieve multimodal deformation of the robotic arm. A filled circle denotes actuation of a given fiber, while an empty circle denotes no actuation of that fiber. The arm is fixed at its top end for all simulations. E) Schematic of transitioning of the robotic arm between different deformation modes, starting from pure bending (red) and transitioning to a coupled bending and twisting mode (purple).

In this work, we propose a multi-contractible-fiber design strategy for elephant trunk-inspired soft robotic arms (Figure 1C). The artificial muscle fibers have programmable orientations and are made of liquid crystal elastomers (LCEs), which can contract with certain strains upon Joule heating. A soft inactive elastomer rod is taken to be the artificial elephant "trunk", with a discrete number of LCE artificial muscles patterned in straight and/or helical manners along it. Despite recent works using LCE for impressive deformation of soft cylindrical actuators,[9a–c] the present work focuses on the general patterning of contractible fibers onto an inactive cylinder to warrant multimodal deformation and transitioning between modes for continuous movements through selective fiber actuation, with the fiber material not being limited to LCE. In this way, the thousands of muscle fibers which determine the movements of the elephant trunk can be simplified into only several artificial muscle fibers with controllable strains. Contraction of a single helical fiber leads to a twisting deformation, while contraction of a straight fiber results in pure bending. Moreover, with the discrete number of artificial muscles, the combination of selectively addressable artificial muscle fibers with different orientations and controllable strains enables multimodal deformations (Figure 1D) as well as transitioning between modes (Figure 1E) for functional movements of the robotic arms, similar to those of an elephant trunk. Figure 1D depicts the multimodal

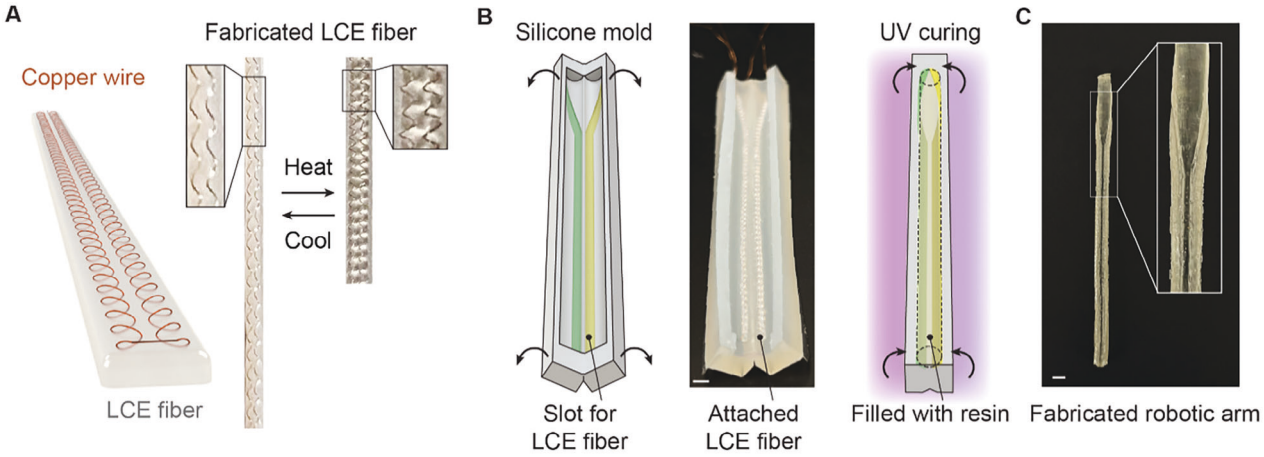

Figure 2. LCE fiber and robotic arm fabrication. A) Schematic (left) and experimental images (right) of an LCE fiber with embedded coiled copper wires. Upon heating and cooling, the LCE exhibits large reversible strains. B) Schematic (left) of the mold for a robotic arm with slots (green and yellow) for the LCE fibers. Experimental image (middle) of the mold with the LCE fibers placed inside. Schematic (right) of the closed mold with placed LCE fibers and resin under UV curing. C) Experimental image of the fabricated robotic arm after being removed from the mold. Scale bars: 4 mm.

deformations and their transitions enabled by selective and sequential actuation. Considering the arm design in Figure 1C with one straight fiber (blue) and one helical fiber (orange) and starting from the initial straight state, the arm can directly achieve bending, coupled bending and twisting, or twisting through selective actuation of the straight fiber (blue), straight and helical fibers (blue and orange), or only the helical fiber (orange), respectively (Figure 1D). Multi-step or sequential actuation can be performed to switch between deformation modes. In addition to this, the arm can transition between different modes (Figure 1E) by carefully controlling the strain in each fiber, creating functional paths or movements between different configurations.

Through experiments, finite element analysis (FEA), and a theoretical model, we systematically study longitudinal and helical LCE fiber design for achievable deformations, mode transitions, and the reachability of elephant trunk-inspired soft robotic arms. We parametrically investigate fiber geometry and layout for 2-fiber robotic arms and characterize the tilting and bending behaviors of these arms. Additionally, through controlled varying of strains in the muscle fibers, transitioning between different deformation modes as well as task-oriented movements such as manipulating and swinging of an object in air is demonstrated for a 2-fiber robotic arm. Lastly, a 3-fiber robotic arm with a longitudinal fiber and two opposite helical fiber arrangement analogous to that of an actual elephant trunk is explored. The remarkably wide range of achievable deformations and the reachability of the 3-fiber arm are discussed in detail, alongside demonstrations of the arm transitioning between different deformation modes for continuous movements. We anticipate that our design and actuation strategy will serve as a robust method to realize bioinspired and biomimetic actuators for various engineering applications.

2. Results and Discussion

2.1. Fabrication of Soft Robotic Arms

The artificial muscle fiber of the robotic arm is made of LCE, which can exhibit large and reversible strains along a programmed direction upon heating and cooling.[12] In the material preparation stage, the liquid crystal mesogens of the LCE are aligned in a certain direction such that the material will experience macroscopic contraction along this direction when heated (Figure 1C). Here, direct ink writing (DIW) is used to achieve alignment of mesogens in the LCE along the print path during extrusion.[13] To achieve Joule heating, coiled copper wires are embedded into the printed LCE fibers before their curing by UV light (see the Experimental Section and Figure S1, Supporting Information for more details). Schematics and experimental images of the LCE fiber with embedded coiled wires are shown in **Figure 2A**. The LCE utilized in this work has a shear modulus estimated as $G = 473$ kPa and, with embedded copper coils, can have repeatable strains up to −33% upon heating (see Figure S2, Supporting Information for mechanical characterizations of the LCE).

Once the LCE fibers with copper coils are fabricated, silicone molds (Figure 2B) are made based on the specific robotic arm design, which allow for the casting of the inactive elastomer rod ($G = 42.6$ kPa, characterization in Figure S2, Supporting Information). The molds contain slots along which the LCE fibers are gently adhered (Figure 2B, middle). Finally, the mold is closed and filled with UV-curable resin (Figure 2B, right). Upon UV curing of the material, the robotic arm in its entirety is removed from the mold, as pictured in Figure 2C. The inactive rod for all robotic arms in this work has a diameter of 4 mm and length of 90 mm, and the fiber thickness and width are constant across all designs (0.4 mm and 1.7 mm, respectively). The present inactive rod material was chosen based on its easy deformability, stability under high temperatures (see Figure S2, Supporting Information for characterization), and its ability to bond with LCE without delamination during cyclic actuation (see Figure S3, Supporting Information for cyclic actuation tests), however, a wide range of inactive materials are applicable to use for these soft robotic arms, and their deformation can be conveniently and accurately predicted with FEA. Additional details on the fabrication of the robotic arms are provided in the Experimental Section and Figure S1 of the Supporting Information.

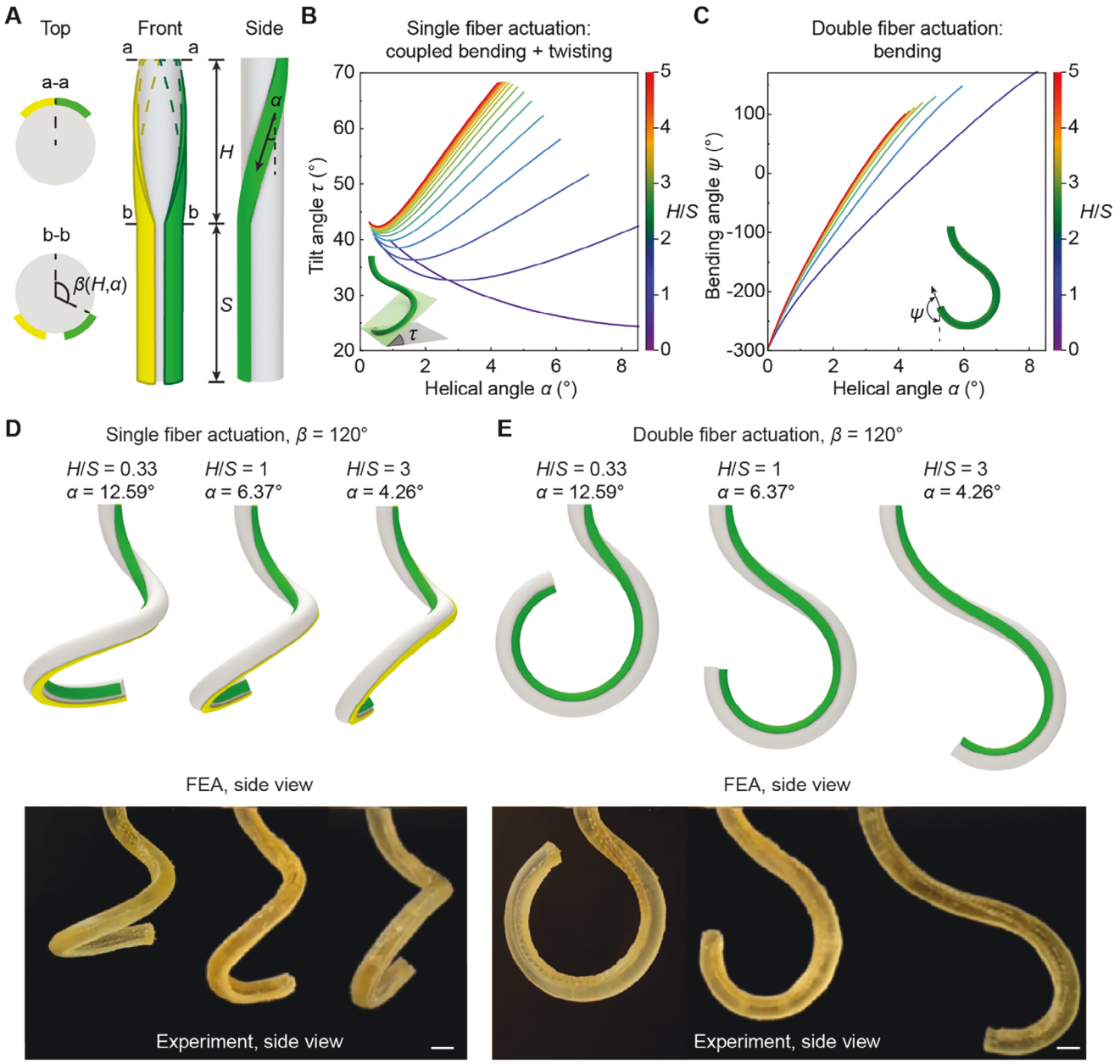

Figure 3. Multimodal deformation of the robotic arm by fiber design. A) Schematic top, front, and side views of the 2-fiber arm design with LCE fiber portions having helical (*H*) and straight (*S*) orientations. α and β denote the helical angle and revolution angle of the helical portion, *H*, respectively. Section view a-a is of the rod cross-section at the top end, while section view b-b is of the rod cross-section where *H* and *S* portions meet. B) Theoretical predictions from the AF model of tilt angle (τ) versus helical angle (α) versus H/S for single fiber actuation. C) Theoretical predictions from the AF model of bending angle (ψ) versus helical angle (α) versus H/S for double fiber actuation. FEA (top) and experimental (bottom) results of robotic arms with $\beta = 120°$ for $H/S = 0.33$, 1, 3 under D) single fiber actuation and E) double fiber actuation. Scale bars: 4 mm.

2.2. Tunable Deformation of Robotic Arms Via Fiber Design

To explore the design space and characterize the deformations of the robotic arms capable of mimicking elephant trunks, we first consider an arm with two symmetric fibers (see **Figure** 3A). We utilize the active filament (AF) theoretical model (detailed information provided in the Supporting Information and Figure S4, Supporting Information) involving a tubular structure with contractible fibers to investigate how fiber geometry influences the achievable deformation modes.[14] For this section, in the experimental and FEA implementations, the actuation strain of the LCE fibers is fixed to −27% (corresponding to heating to roughly 140 °C, see Figure S2 (Supporting Information) for the relation between actuation strain and temperature) and the fiber width and thickness are constant across designs (see the Experimental Section for details). The 2-fiber arm, as shown in Figure 3A, is characterized by two identical LCE fibers (yellow and green) of opposite handedness with both straight (*S*) and helical (*H*)

portions which meet at the fixed end of the arm (as noted in section view a-a in Figure 3A). H and S characterize the length of the helical and straight fiber portions, respectively, along the rod. The helical angle of the fiber in the H portion is characterized by α, and the revolution angle of the fiber by β. Note that α, β, and H are dependent on one another.

Since contraction of a single straight fiber produces bending and contraction of a single helical fiber produces twisting, contraction of a single fiber with both helical and straight portions results in a coupled bending and twisting mode, such as the inset shown in Figure 3B. On the other hand, by contracting both fibers at once at the same strain, a pure bending mode is achieved due to the symmetric fiber arrangement, such as the configuration shown in the inset of Figure 3C. Thus, the 2-fiber arm is capable of a coupled bending and twisting mode, as well as a pure bending mode. To describe the deformed configurations of the arm under single or double fiber actuation, a tilt angle τ and a bending angle ψ, are defined respectively in the insets of Figure 3B,C. Here, the tilt angle τ is the angle between the plane of the bending loop of the S portion with respect to a reference horizontal plane. The tilt angle is used to characterize the arm's orientation caused by the twisting of portion H. The same plots, but in terms of fiber revolution angle, β, are provided in Figure S5 (Supporting Information).

To investigate the influence of fiber geometry on the final deformation of the arm, we conduct parametric studies via the AF model by varying the H/S ratio and the helical angle α of the H portion while fixing the fiber activation. Figure 3B shows the deformation of the robotic arm under single fiber actuation, characterized by τ versus α versus H/S. Particularly, for a constant α and an increasing H/S, τ also tends to increase. The tilt angle τ first decreases and then gradually increases with the helical angle α for a given H/S. Note that the range of α, starting from a very small value, is not the same for all H/S, as cases where intersection of fibers exists are not considered; the fiber designs with relatively large H/S have smaller α ranges. A plot with an expanded α range and additional discussion are provided in Figure S6 (Supporting Information).

Pure bending can be achieved by actuating both fibers at once with the same strain, as the twisting of the helical portions effectively cancel each other out when contracted simultaneously. The bending direction is determined by the axis of symmetry between the two S fiber portions. To characterize the localized bending near the tip, a bending angle, ψ, is defined as the angle between the axial direction of the tip of the robotic arm and the vertical. The bending angle results computed from the AF model are plotted versus α and H/S in Figure 3C. For a given α, greater ψ is achieved with greater H/S while, for a given H/S, ψ increases with increasing α. Thus, the extent of bending, which is akin to the extent of wrapping around an object, can also be designed through fiber geometry. Additional results from the AF model, such as the bending angle with respect to fiber activation and the loop formed during bending, are discussed in Figures S7 and S8 (Supporting Information), respectively.

FEA and experimental implementations of three different fiber geometries are shown in Figure 3D,E for the fixed actuation strain of −27%, where H/S are 0.33, 1, and 3, while the H portion revolution β is held constant at 120°, and α are 12.59°, 6.37°, and 4.26°, respectively. Side views of FEA and experimental results for single fiber actuation and double fiber actuation of these arms are provided in Figure 3D,E (see also Movies S1 and S2, Supporting Information), respectively. We see good agreement between FEA simulations and experiments. In these examples, the fibers are heated to roughly 140 °C under an applied current of 0.85 – 1.0 A to the coiled copper wires in each fiber, and the actuated configuration at this temperature is shown in the figure. The copper wire resistance among all fibers for a given arm is the same, while the resistance varied between 3.4 – 4.0 Ω across different robotic arm designs. Thermal IR imaging information is provided in Figure S9 (Supporting Information), and additional views from FEA as well as comparison between FEA and AF model results are provided in Figures S10 and S11 (Supporting Information), respectively. For the fixed β of 120°, the tilt angle increases with H/S, with values of 30°, 38°, and 45° at their actuated states (−27% fiber strain), respectively, for H/S of 0.33, 1, and 3. Quantitative information from FEA on the deformed strain and reachability of these arms is provided in Figure S12 (Supporting Information). The different tilt or orientation of the robotic arm in space can potentially be useful for grasping differently oriented objects, while the tunable position of the loop of the arm can be useful for reaching or grabbing objects in different positions relative to the trunk.

2.3. Tunable Deformation and Movement of the Robotic Arm through Varied Fiber Strain

Elephants adapt different strategies to grasp and lift objects by bending or wrapping around objects in different planes. For example, in **Figure 4A** (images from[6b]), the distal end of the elephant trunk bends in a nearly horizontal plane to grasp an object, while it can also bend in oblique or vertical planes to pick up objects. Grasping an object in one plane and then reorienting the trunk while holding the object is also a very common behavior that can be replicated by the soft robotic arm by varying the strain in the LCE fibers. To realize the task-oriented trunk motion, the transitioning between deformations is investigated by actively controlling the strain in selected fibers, which produces functional movements appropriate for the grasping and moving or swinging of objects.

To demonstrate the change in orientation of the robotic arm with fiber strain, we use a 2-fiber robotic arm design with $H/S = 0.33$ and $\alpha = 12.59°$ ($\beta = 120°$, Figure 4B). The reorientation is achieved by sequential fiber actuation. As shown through FEA results (side view) in Figure 4C, changing the actuation strain in one fiber leads to different actuated states of the arm. The transitioning between different deformation modes is achieved by continually changing the LCE strain. Starting from actuating only fiber 1 (yellow) to −27% strain (left in Figure 4C), the robotic arm shows a coupled bending and twisting mode. When the strain in fiber 2 (green) is gradually ramped from 0% to −14% strain and then to −27% strain, the arm orients from coupled bending and twisting to pure bending (or bending in an oblique plane to bending in a vertical plane) once both fibers are actuated to −27% strain. A plot of the tilt angle, τ, versus H/S versus activation for $\beta = 120°$ is provided in Figure S13 (Supporting Information), for context on the reorientation of robotic arms of different geometries than the one considered in this figure. The reorientation

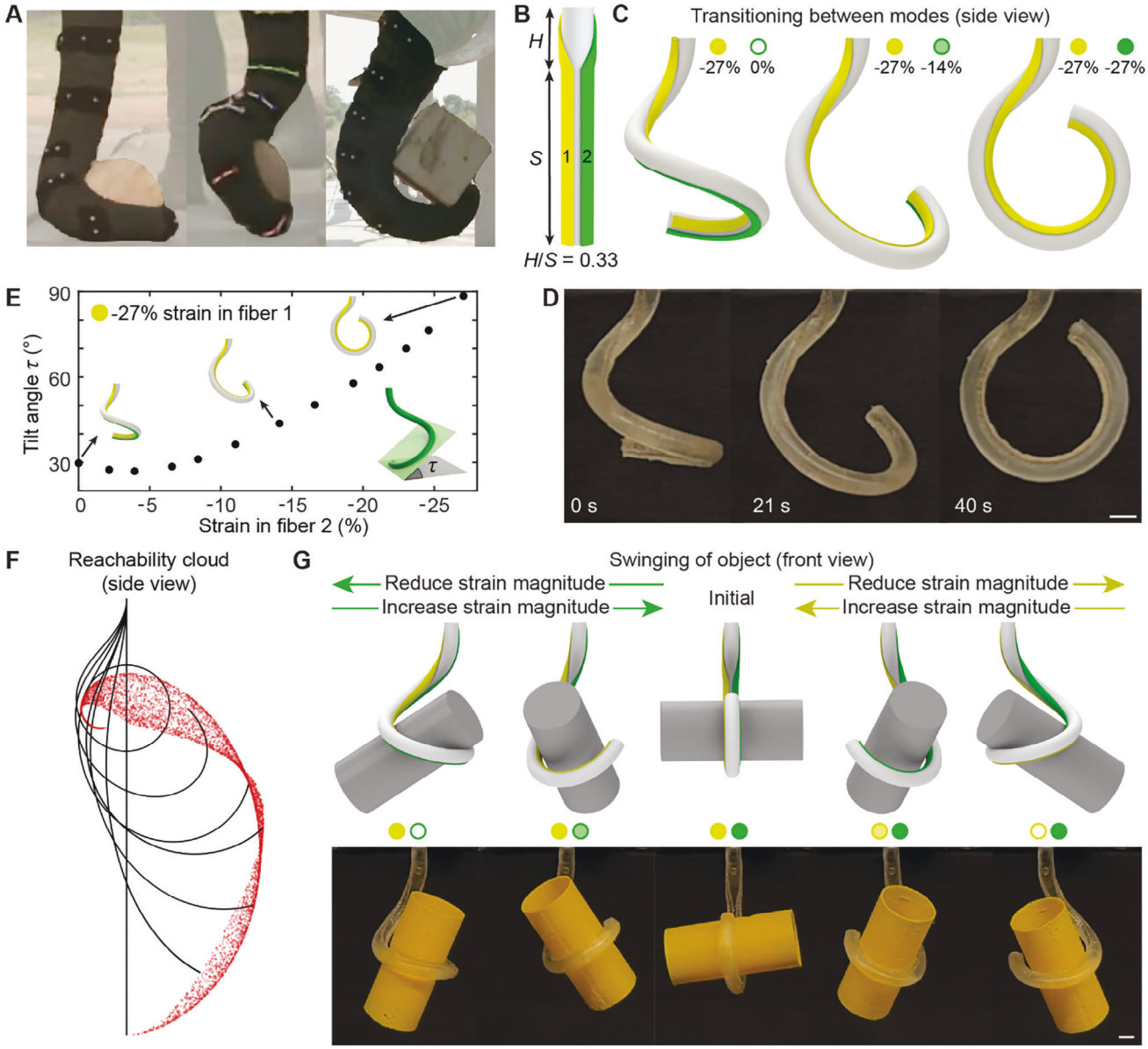

Figure 4. Tunable deformation of the robotic arm by fiber contraction. A) Images of an elephant trunk grasping various objects (Adapted with permission, CC-BY.[6b]). The trunk can reorient its bending to grasp each object. B) Schematic of the 2-fiber robotic arm design, with $H/S = 0.33$, $\alpha = 12.59°$. The LCE fibers are denoted as fiber 1 (yellow) and fiber 2 (green). C) FEA and D) experimental results of the robotic arm transitioning from coupled bending and twisting modes to a pure bending mode. The circles denote the actuated fiber, with fiber 1 actuated at a constant strain of −27% and fiber 2 gradually changed from 0% to −27% strain. E) Tilt angle, τ, versus strain of fiber 2 from FEA while fiber 1 is held constant at −27% strain. F) Theoretical prediction from the AF model of the cloud of reachable points for the tip of the robotic arm under different combinations of contraction in each fiber, with a maximum deformed fiber strain of −33%. G) Demonstration via FEA (top) and experiment (bottom) of the arm lifting an object and swinging it from right to left by varying the strain in each fiber. The object is adhered to the robotic arm. Scale bars: 4 mm.

of the arm is validated experimentally, as shown in Figure 4D, where only fiber 1 is actuated at 0 s. As the strain in fiber 2 is ramped to the same magnitude as fiber 1, the amount of twist in the arm decreases, and the bending portion of the arm is reoriented until pure bending is achieved at 40 s (see Movie S3, Supporting Information). The tilt angle, τ, of the arm from FEA is characterized during this process, and it is seen that τ decreases slightly upon actuating the second fiber but increases nearly linearly with the decreasing strain after this region (Figure 4E). The configurations from Figure 4C are placed along the graph for reference.

The reachability cloud of the arm, constructed by the reachable points of the tip of the arm under different combinations of strain in each fiber, are predicted by the AF model as shown in Figure 4F (see Figure S14, Supporting Information for additional views of the cloud). The deformed strain in each fiber of the reachability cloud ranges from 0% to −33%. Importantly, the majority of reachable points are located toward the front side of

the arm, where the two *S* portions of the fibers are located. In the next section, a robotic arm design with more expansive reachability will be explored. Lastly, to demonstrate the utility of the robotic arm's ability to reorient in space, the lifting and swinging of a cylindrical object is performed experimentally and via FEA (Figure 4G, see Movie S3, Supporting Information). First, both fibers are actuated to −27% strain to lift the object up via pure bending to its "initial" state. Then, by reducing the strain magnitude in fiber 1 to 0%, the arm swings to the right, in turn rotating the object with it. The arm returns to its initial pure bending state by gradually returning to −27% strain in both fibers, and then swings to the left upon reducing the strain magnitude in fiber 2 to 0%. Thus, we have demonstrated functionality of the arm in its ability to lift and swing objects through the sequential actuation and controlled strain of the LCE fibers. The strength and robustness of the arm are assessed by performing lifting tests with a series of different weights (1 g, 2 g, and 5 g, Figure S15, Supporting Information) and a 20-cycle actuation test (Figure S3, Movie S2, Supporting Information).

2.4. Bioinspired 3-Fiber Robotic Arm Design with Extensive Reachability

The arrangement of muscle fibers in the elephant trunk, namely, the longitudinal muscles along the front side and oblique muscles concentrated to the back side (**Figure 5**A), which contribute to the trunk's wide array of achievable deformations, can be simplified to only a discrete number of LCE fibers in our soft robotic system. In this section, a 3-fiber arrangement is introduced which closely mimics the muscles in an elephant trunk for multimodal deformations. As shown in Figure 5B, this robotic arm design has one straight fiber (blue) and two helical fibers of opposite handedness (yellow, green) wrapping toward the front of the arm with $\alpha = 2.88°$ ($\beta = 108°$). This simple configuration of LCE fibers roughly replicates the complex arrangement of longitudinal and oblique muscles in an elephant trunk, as compared to the schematic of muscle fibers in an elephant trunk's anatomy shown in Figure 5A. Although the robotic arm contains only three fibers, the achievable deformations are remarkably rich.

Several achievable deformation modes of the 3-fiber arm from FEA (side view) are shown in Figure 5C and Movie S4 (Supporting Information). Translucent configurations of the arms are given at approximately −8%, −17%, and −22% strains, with the actuated fiber(s) denoted by the colored circle(s), while the configuration at −27% strain is opaque, showing the evolution of the arm's shape with the different fiber actuation strains. Actuation of the straight (blue) fiber yields pure bending of the whole arm, while actuation of all three fibers results in pure bending localized at the distal end of the arm. Twisting of the arm is achieved through actuation of a single helical (green or yellow) fiber, and coupled bending and twisting is achieved when both the straight (blue) and helical (green or yellow) fibers are actuated. Corresponding experimental results (side view) are shown in Figure 5D for the arm when the designated fibers are heated to roughly 140 °C (corresponding to −27% strain). It can be seen that the experimental results closely follow those from FEA. Results for the deformed configuration when the two helical fibers are simultaneously actuated are provided in Figure S16 (Supporting Information). Additionally, front, isometric, and top views of the FEA corresponding to those in Figure 5C are provided in Figure S17 (Supporting Information), as well as deformed strain information from FEA in Figure S18 (Supporting Information), and comparison to the AF model results in Figure S19 (Supporting Information).

One main advantage of the 3-fiber robotic arm design is its reachability in various directions. The reachable points of the tip of the robotic arm under different combinations of activation in the fibers are predicted by the AF model, as shown in Figure 5E. For the given 3-fiber design, seven general fiber actuation combinations exist. Within each combination, the strain in each fiber can be varied. Front and side views of the plots of reachable points for each combination are provided in Figure 5E. For the case of single fiber actuation (Figure 5E,i), the reachable points of the arm fall along a single curve for different LCE fiber activations. More interesting are the clouds of reachable points for multi-fiber actuation (Figure 5E,ii,iii). From the blue & yellow and blue & green fiber actuation clouds, it can be seen that the reachable points, when straight and helical fibers are actuated, lie roughly in front of and to the side of the arm where the helical fiber resides. On the other hand, the yellow & green fiber actuation cloud contains reachable points mostly spanning the back side of the arm. Thus, when different magnitudes of contraction (deformed strain range of 0% to −21% (yellow & green fibers) or 0% to −25% (blue fiber)) are applied to all three fibers (Figure 5E,iii), the arm can reach in nearly all directions, akin to a real elephant trunk. See Figure S20 (Supporting Information) for corresponding side, front, and top views of all reachable point plots in Figure 5E.

To further demonstrate the reachability of the robotic arm, as well as the ability of the arm to have complex motion paths and movements between different deformation modes, we present two examples (Figure 5F,i,ii) of multi-step sequential actuation of the 3-fiber arm. Here, we consider a movement to be complex if it involves multiple deformation modes (bending, twisting, and combined modes) and if the arm moves along multiple paths. The first example, Figure 5F,i, shows FEA results of the arm performing a series of movements concentrated on its right side, first by achieving a clockwise twisting motion (mode 1) to its front, then transitioning to a counter-clockwise twist (mode 2), and finally reaching backward and to the right (mode 3). Note that this series of deformations involves the actuation of all three fibers. The transitions between deformation modes demonstrate the versatility and range of motion of the arm and its potential ability to perform complex tasks in a localized region. The LCE fiber control scheme for this series of movements is detailed in Table S1 (Supporting Information), and the video of this process is provided in Movie S4 (Supporting Information). Last, to show the reachability of the arm to its front, back, left, and right, FEA of the arm is performed, where the arm first bends forward (mode 1) and then reaches backward via pure bending (mode 2), followed by sweeping along the arm's backside to the right (mode 3), then center (mode 2), and left (mode 4), as shown in Figure 5F,ii. An experimental implementation of this deformation process is shown in Figure S21 and Movie S4 (Supporting Information). Quantitative information from FEA on the reachable bounds of the arm during the actuation sequence from Figure 5F,ii is provided in Figure S22 (Supporting Information). The specific LCE fiber control sequence is provided in Table S1 (Supporting

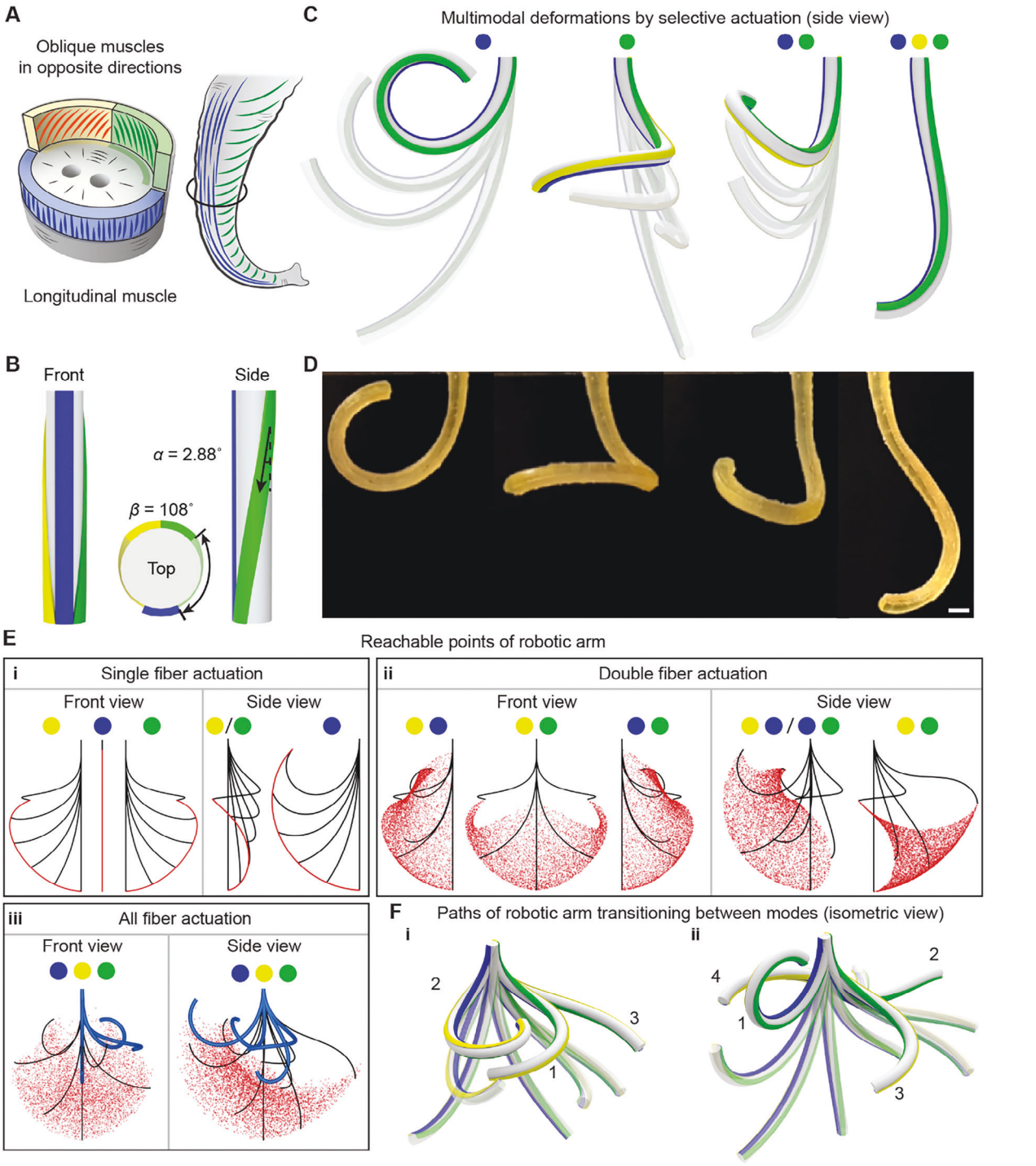

Figure 5. Bioinspired 3-fiber robotic arm design with multimodal deformation and extensive reachability. A) Muscle fiber schematic of an elephant trunk anatomy, including longitudinal (blue) and oblique (yellow, green) muscle fibers with opposite handedness. B) Schematic front, side, and top views of a 3-fiber robotic arm design with one straight fiber (blue) and two helical fibers (yellow and green) with reverse handedness and $\alpha = 2.88°$, $\beta = 108°$. Multimodal deformations of the robotic arm achieved from C) FEA and D) experiments under selective fiber actuation. Pure bending is achieved from the blue fiber actuation, twisting is achieved from the green fiber actuation, coupled bending and twisting from simultaneous blue and green fiber actuation, and bending localized at the distal end results from the simultaneous actuation of all fibers. Scale bar: 4 mm. E) Theoretical predictions from the AF model (front and side views) for the cloud of reachable points of the tip of the 3-fiber arm under (i) single fiber actuation, (ii) double fiber actuation, and (iii) all fiber actuation. The four actuated configurations corresponding to those in subfigure C and D are highlighted in (iii). The maximum deformed strain is −25% in the blue fiber and −21% in the yellow and green fibers. F) Configurations from FEA of the robotic arm transitioning between different deformation modes by controlling the strain in each fiber. The order of configurations is numbered, and the translucent arms depict the shape of the arm between configurations.

Information), and the FEA results are shown in Movie S4 (Supporting Information). In summary, the 3-fiber robotic arm has a minimalistic arrangement of muscle fibers analogous to that of an actual elephant trunk and is capable of a wide range of multimodal deformations through selective actuation of the fibers, as well as complex motion paths achieved through sequential actuation, with broad reachability achieved throughout these processes.

3. Conclusion

In summary, we have introduced a design and accompanying actuation strategy for soft robotic arms capable of multimodal, elephant-like deformations, functional movements, and deformation transitions through a combination of experiments, FEA, and a theoretical model. Our robotic arms are composed of soft, inactive rods with LCE fibers patterned longitudinally or helically along their length, which can be actuated selectively via Joule heating. The simple and rationally designed layout of helical and straight LCE fibers can lead to a remarkably diverse set of achievable deformations, such as pure bending, twisting, coupled bending and twisting, as well as distally concentrated bending, via selective and sequential fiber actuation. Parametric studies on the LCE fiber geometry and layout are performed for 2-fiber robotic arm designs, to characterize the tilting, bending, and reaching behavior of the arms. Additionally, we propose a 3-fiber robotic arm which has a greatly simplified muscular arrangement inspired by the complex architecture of muscle fibers in the elephant trunk. With only a discrete number of LCE fibers, the unique 3-fiber arrangement can replicate deformations similar to an actual elephant trunk. In addition, the arm has broad reach and can perform complex sequences of movement when the LCE fibers are subjected to different actuation strains. We anticipate that the design and actuation strategy concepts presented in this work will inspire future actuator design for soft, high-DOF actuators used in a variety of applications.

4. Experimental Section

Material and Robotic Arm Fabrication: *LCE fibers*: To prepare the LCE ink, liquid crystal mesogens (2-Methyl-1,4-phenylene bis(4-((6-(acryloyloxy)hexyl)oxy)benzoate)) (RM 82, BOC Sciences, USA) and (1,4-Bis-[4-(3-acryloyloxypropyloxy)benzoyloxy]−2-methylbenzene) (RM 257, BOC Sciences, USA) were mixed in a weight ratio of 2.7:1. Next, the spacer (2,2-(Ethylenedioxy)diethanethiol) (EDDET, Sigma Aldrich, USA) and antioxidant (2,6-Di-tert-butyl-4-methylphenol) (BHT, Sigma Aldrich, USA), were added at 22.5 wt% and 2.25 wt% to the total weight of mesogens. After melting all components at 80 °C for 45 min, the catalyst triethylamine (TEA, Sigma Aldrich, USA) and photoinitiator Irgacure 819 (Sigma Aldrich, USA) were added at 1.6 wt% and 1.8 wt%, respectively, to the total weight of mesogens. The mixture was stirred for 3 min with a magnetic stir bar at 80 °C, then oligomerized in an oven at 80 °C for 15 min, and next transferred to a 10 mL syringe barrel (Nordson EFD, USA), and heated again in a vacuum oven at 80 °C for 20 min. The ink was finally defoamed in a planetary mixer (AR-100, Thinky, USA) at 2200 rpm for 6 min to remove trapped air.

A customized 3D printer was used for DIW of the LCE fibers. 90 mm-long fibers with longitudinal alignment, a width of 1.7 mm, and thickness of 0.4 mm were printed. 44 AWG (≈50 µm diameter) copper wire was coiled, with coil diameter of 0.5 mm, and stretched such that there were 0.68 coils mm^{-1} along the fiber. A single wire with two rows of coils was embedded in each LCE fiber, and the fibers were then cured with UV light for 10 min (see Figure S1A, Supporting Information).

Inactive Elastomer Rod: The liquid resin for the inactive elastomer rod was created by mixing monomer butyl acrylate (Sigma Aldrich, USA), a commercial UV-curable phenoxyethyl acrylate monomer (Ebecryl 114, Allnex, USA), and a commercial UV-curable urethane oligomer (Ebecryl 8413, Allnex, USA) in a weight ratio of 12:7:1. Photoinitiator Irgacure 819 (Sigma Aldrich, USA) was added at 2 wt% to the total weight of the resin, and the resin was mixed manually for 10 min at 80 °C until homogeneous.

Molding: Silicone molds (Ecoflex-0030, Smooth-On, Inc., USA) were created in order to fabricate the soft actuator. The mold was an inverse of the soft actuator design; it included the cavity of a 4 mm diameter by 90 mm long cylinder with 0.4 mm thick slots along the cylinder, patterned in helical or longitudinal manners according to the specific fiber design of the given robotic arm. See Figure S1B (Supporting Information) for details on silicone mold fabrication. By inserting the fabricated LCE fibers into the slots in the mold, the orientation of the LCE fibers was fixed. The inactive elastomer resin was then poured into the mold and UV light was shined on the semi-transparent mold for 15 minutes. During that time, the inactive rod cured while also bonding to the LCE fibers. Once removed from the mold, the soft robotic arm was fully fabricated.

Joule Heating: In all experimental implementations, Joule heating was used as the method to actuate the LCE fibers. The copper wires embedded into the LCE fibers were connected to an external power supply, through which current could be applied to the wires in each individual fiber. The LCE fibers were conductively heated as a current of 0.85 – 1.0 A was applied to each wire being heated, and the temperature of the LCE fibers was monitored with an IR thermal camera (Fotric 348A, Fotric Inc., USA). Depending on the specific resistance and applied current, the arms were heated for 1 to 2 minutes to deform from the initial to actuated state while requiring roughly 5 minutes to cool from 140 °C to room temperature under ambient conditions. More information on the IR imaging is provided in Figure S9 (Supporting Information), and the wire resistance for the fibers in each arm ranged between 3.4 – 4.0 Ω.

FEA Simulations: The commercial software ABAQUS 2021 (Dassault Systèmes, France) was used for the FEA of the robotic arm actuation, in which the LCE fibers were simulated to contract under applied temperatures due to defined orthotropic expansion coefficients (provided in Table S2, Supporting Information). Linear elastic and hyperelastic material models were used for the LCE and the inactive elastomer rod, respectively, with the C3D8H element used for the whole model. Detailed information on all FEA simulations are provided in the Supporting Information.

Supporting Information

Supporting Information is available from the Wiley Online Library or from the author.

Acknowledgements

S.L., J.L.-Y., B.K., S.W., E.K., and R.R.Z. acknowledge support from NSF Award CMMI-2318188. S.L., J.L.-Y., S.W., and R.R.Z. acknowledge support from NSF Career Award CMMI-2145601 and ARO ECP Award W911NF-23-1-0176. Part of this work was performed at the Stanford Nano Shared Facilities (SNSF), supported by NSF Award ECCS-2026822.

Conflict of Interest

The authors declare no conflict of interest.

Author Contributions

E.K., R.R.Z. performed conceptualization. S.L., J.L.-Y., B.K., S.W. performed methodology. S.L., J.L.-Y., S.W. performed investigation. S.L., J.L.-Y., B.K.,

S.W. performed visualization. S.L., B.K. performed formal analysis. S.L., J.L.-Y., B.K. performed validation. E.K., R.R.Z performed funding acquisition, project administration, supervision. S.L., B.K wrote the original draft .S.L., J.L.-Y., B.K., S.W., E.K., R.R.Z wrote – review and edited the original draft.

Data Availability Statement

The data that support the findings of this study are available from the corresponding author upon reasonable request.

Keywords

elephant trunks, functional movements, liquid crystal elastomers, multimodal deformations, soft actuators, soft robotic arms

Received: January 8, 2024
Revised: February 14, 2024
Published online: February 28, 2024

[1] M. Li, A. Pal, A. Aghakhani, A. Pena-Francesch, M. Sitti, *Nat. Rev. Mater.* **2022**, *7*, 235.

[2] a) Z. Zhang, Y. Long, G. Chen, Q. Wu, H. Wang, H. Jiang, *Sci. Adv.* **2023**, *9*, eadg1203; b) Y. Hong, Y. Chi, S. Wu, Y. Li, Y. Zhu, J. Yin, *Nat. Commun.* **2022**, *13*, 530; c) N. R. Sinatra, C. B. Teeple, D. M. Vogt, K. K. Parker, D. F. Gruber, R. J. Wood, *Sci. Rob.* **2019**, *4*, eaax5425; d) J. Shintake, V. Cacucciolo, D. Floreano, H. Shea, *Adv. Mater.* **2018**, *30*, 1707035.

[3] a) Y. Tang, Y. Chi, J. Sun, T.-H. Huang, O. H. Maghsoudi, A. Spence, J. Zhao, H. Su, J. Yin, *Sci. Adv.* **2020**, *6*, eaaz6912; b) X. Qian, Y. Zhao, Y. Alsaid, X. Wang, M. Hua, T. Galy, H. Gopalakrishna, Y. Yang, J. Cui, N. Liu, M. Marszewski, L. Pilon, H. Jiang, X. He, *Nat. Nanotechnol.* **2019**, *14*, 1048; c) M. Yang, Y. Xu, X. Zhang, H. K. Bisoyi, P. Xue, Y. Yang, X. Yang, C. Valenzuela, Y. Chen, L. Wang, W. Feng, Q. Li, *Adv. Funct. Mater.* **2022**, *32*, 2201884; d) S. Wu, Q. Ze, J. Dai, N. Udipi, G. H. Paulino, R. Zhao, *Proc. Natl. Acad. Sci. USA* **2021**, *118*, e2110023118; e) S. Naficy, R. Gately, R. Gorkin III, H. Xin, G. M. Spinks, *Macromol. Mater. Eng.* **2017**, *302*, 1600212.

[4] a) Q. Ze, S. Wu, J. Dai, S. Leanza, G. Ikeda, P. C. Yang, G. Iaccarino, R. R. Zhao, *Nat. Commun.* **2022**, *13*, 3118; b) Y. Kim, G. A. Parada, S. Liu, X. Zhao, *Sci. Rob.* **2019**, *4*, eaax7329; c) M. Cianchetti, C. Laschi, A. Menciassi, P. Dario, *Nat. Rev. Mater.* **2018**, *3*, 143.

[5] W. M. KIER, K. K. SMITH, *Zool. J. Linn. Soc.* **2008**, *83*, 307.

[6] a) L. L. Longren, L. Eigen, A. Shubitidze, O. Lieschnegg, D. Baum, J. A. Nyakatura, T. Hildebrandt, M. Brecht, *Curr. Biol.* **2023**, *33*, 4713; b) P. Dagenais, S. Hensman, V. Haechler, M. C. Milinkovitch, *Curr. Biol.* **2021**, *31*, 4727.

[7] a) Q. Guan, J. Sun, Y. Liu, N. M. Wereley, J. Leng, *Soft Rob.* **2020**, *7*, 597; b) M. Schaffner, J. A. Faber, L. Pianegonda, P. A. Rühs, F. Coulter, A. R. Studart, *Nat. Commun.* **2018**, *9*, 878; c) L. Yue, S. Macrae Montgomery, X. Sun, L. Yu, Y. Song, T. Nomura, M. Tanaka, H. Jerry Qi, *Nat. Commun.* **2023**, *14*, 1251; d) B. Yang, R. Baines, D. Shah, S. Patiballa, E. Thomas, M. Venkadesan, R. Kramer-Bottiglio, *Sci. Adv.* **2021**, *7*, eabh2073; e) S. Y. Kim, R. Baines, J. Booth, N. Vasios, K. Bertoldi, R. Kramer-Bottiglio, *Nat. Commun.* **2019**, *10*, 3464; f) F. Connolly, P. Polygerinos, C. J. Walsh, K. Bertoldi, *Soft Rob.* **2015**, *2*, 26.

[8] a) R. V. Martinez, J. L. Branch, C. R. Fish, L. Jin, R. F. Shepherd, R. M. D. Nunes, Z. Suo, G. M. Whitesides, *Adv. Mater.* **2013**, *25*, 205; b) J. Zou, M. Feng, N. Ding, P. Yan, H. Xu, D. Yang, N. X. Fang, G. Gu, X. Zhu, *Nat. Sci. Rev.* **2021**, *8*, nwab048; c) J. Yan, X. Zhang, B. Xu, J. Zhao, *Soft Rob.* **2018**, *5*, 527; d) I. De Falco, M. Cianchetti, A. Menciassi, *Bioinspir. Biomim.* **2017**, *12*, 056008; e) W. McMahan, V. Chitrakaran, M. Csencsits, D. Dawson, I. D. Walker, B. A. Jones, M. Pritts, D. Dienno, M. Grissom, C. D. Rahn, presented at IEEE Int. Conf. on Robotics and Automation, ICRA, Orlando, May **2006**.

[9] a) Z. Hu, Y. Zhang, H. Jiang, J.-A. Lv, *Sci. Adv.* **2023**, *9*, eadh3350; b) Q. He, Z. Wang, Y. Wang, A. Minori, M. T. Tolley, S. Cai, *Sci. Adv.* **2019**, *5*, eaax5746; c) X. Qian, Q. Chen, Y. Yang, Y. Xu, Z. Li, Z. Wang, Y. Wu, Y. Wei, Y. Ji, *Adv. Mater.* **2018**, *30*, 1801103; d) M. Kang, Y.-J. Han, M.-W. Han, *Polymers* **2023**, *15*, 1126.

[10] S. Joe, O. Bliah, S. Magdassi, L. Beccai, *Adv. Sci.* **2023**, *10*, 2302080.

[11] a) M. G. B. Atia, A. Mohammad, A. Gameros, D. Axinte, I. Wright, *Adv. Sci.* **2022**, *9*, 2203217; b) J. Zhang, J. Shi, J. Huang, Q. Wu, Y. Zhao, J. Yang, H. Rajabi, Z. Wu, H. Peng, J. Wu, *Adv. Intell. Syst.* **2023**, *5*, 2300048; c) J. Zhang, B. Wang, H. Chen, J. Bai, Z. Wu, J. Liu, H. Peng, J. Wu, *Adv. Mater. Technol.* **2023**, *8*, 2201616.

[12] a) H. Wermter, H. Finkelmann, *e-Polymers* **2001**, *1*, 013; b) K. M. Herbert, H. E. Fowler, J. M. McCracken, K. R. Schlafmann, J. A. Koch, T. J. White, *Nat. Rev. Mater.* **2022**, *7*, 23.

[13] a) C. P. Ambulo, J. J. Burroughs, J. M. Boothby, H. Kim, M. R. Shankar, T. H. Ware, *ACS Appl. Mater. Interfaces* **2017**, *9*, 37332; b) A. Kotikian, R. L. Truby, J. W. Boley, T. J. White, J. A. Lewis, *Adv. Mater.* **2018**, *30*, 1706164.

[14] a) B. Kaczmarski, D. E. Moulton, E. Kuhl, A. Goriely, *J. Mech. Phys. Solids* **2022**, *164*, 104918; b) B. Kaczmarski, A. Goriely, E. Kuhl, D. E. Moulton, *IEEE Robot. Autom. Lett.* **2023**, *8*, 936.